Long-Range High-Resolution Imaging with Silicon-On-Nothing ScAlN pMUTs

Mantalena Sarafianou, David Sze Wai Choong, Daniel Ssu-Han Chen, Duan Juan Goh, Zhang Yao, Jaibir Sharma, Srinivas Merugu, Eldwin Jiaqiang Ng, Joshua En-Yuan Lee .

***Abstract*—This work demonstrates the imaging capabilities of a Silicon-On-Nothing (SON) ScAlN piezoelectric micromachined ultrasonic transducer (pMUT) array by a method of transmit beamforming followed by suitable signal post-processing for 3D image reconstruction. A 2.7MHz pMUT array with 15% Scandium doped Aluminum Nitride as the piezo thin-film was implemented for this demonstration. A total of sixteen 3×3 mm dies consisting of 34×37 pMUT elements per die and operated as dual channels were arranged in an 8-column×2-row array configuration, resulting in a 32-channel experimental system with a 24mm×6mm coverage. In this work, experimental testing using single and multiple 6mm diameter reflectors at a different spacing from each other and a distance of 2.5cm from the array was performed to validate the 3D imaging capabilities of the developed 2D SON ScAlN pMUT array with an attained lateral resolution of 5mm.**

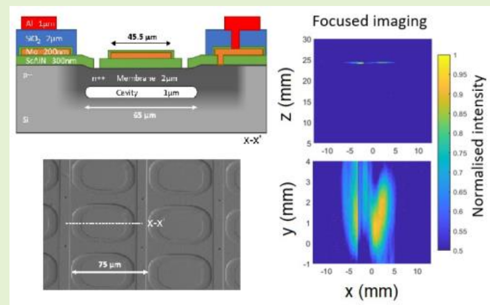

***Index Terms*—Piezoelectric micromachined ultrasonic transducer (pMUT), Phased array, ScAlN, Silicon-On-Nothing, Transmit beamforming, Ultrasonic imaging**

I. Introduction

TO-date, ultrasonic transducers have been used in various applications including but not limited to medical imaging [1], non-destructive testing (NDT) [2], ranging [3], [4], and mid-air haptics [5]. Traditional ultrasonic transducer arrays based predominately on bulk piezoelectric ceramics have been used extensively for imaging; there are several drawbacks associated with them. First, high-resolution imaging is inherently dependent on high frequencies. This is unattainable for piezo-ceramics due to the difficulty in scaling down the size of the arrays [6]. Second, for certain imaging applications such as endoscopy and non-destructive testing (NDT), the need for an array that can fit in small enclosures makes bulk piezo materials unsuitable [7]. A good alternative that could address these design challenges would be piezoelectric micromachined ultrasonic transducer (pMUT) arrays given their small form factor, low-cost, and matured fabrication processes [8]. {PMUTs have attracted significant attention over the past 20 years given their desirable traits such as circuit integration, tighter pitch, good acoustic impedance matching, low driving voltage, high receive sensitivity, and ease of pulse frequency control [9]–[12]. Currently, research on pMUTs for imaging applications has focused on short-range/surface imaging (e.g, fingerprint mapping) [13], [14], defect detection in solid materials [7], and medical imaging [15]–[17]. In the imaging implementations of [13], [14], high-resolution imaging is achieved (100-200µm), but limited to short ranges of a few millimeters. This limitation comes even after some optimization either through mechanical scanning in [13], which is a laborious and time-consuming process or the use of a waveguide in [14], which can only preserve the acoustic pressure for a couple of millimeters axially. In [7], defect detection over long-range distances as far as 3cm can be achieved, but at the cost of lateral resolution (approximately 1cm). In addition, [7] proposed Full Matrix Capture (FMC) for image reconstruction, which could lead to the production of large data files for post-processing, slow scanning speeds, and reduced SNR. Based on this literature review, there is a gap in immersion imaging with pMUT arrays at long ranges, which is the focus of the work presented here. We propose the use of a multi-channel SON ScAlN pMUT array, which consists of multiple dies, for imaging in fluids at distances of 2-3cm with an experimentally achievable lateral resolution of 5mm.

The work presented here focuses on imaging with ScAlN pMUTs, which are fabricated using the Silicon-On-Nothing (SON) process as opposed to the traditional fabrication methodologies by releasing the membranes from Silicon-On-Insulator (SOI) wafers [19], [20]. ScAlN, as also AlN, has certain

This paper manuscript was submitted for review on 7 December 2022. This research was supported by A*STAR under the “Piezo Specialty Lab-in-a-Fab” (Grant No. I1901E0050) and “Nanosystems at the Edge” programme (Grant No. A18A4b0055).

Dr. Mantalena Sarafianou, David S. W. Choong, Duan Juan Goh, Zhang Yao, Dr. Daniel S. H. Chen, Dr. Jaibir Sharma, Srinivas Merugu, Dr. Eldwin Ng, and Dr. Joshua E.-Y. Lee are with the Institute of Microelectronics (IME), A*STAR, 2 Fusionopolis Way, Singapore, 138634 (e-mail: {Mantalena Sarafianou}; {David_Choong}; {Goh Duan Jian}; {Zhang Yao}; {Daniel Chen}; {Sharmaj}; {Merugus}; {Joshua Lee}@ime.a-star.edu.sg)

Dr. Eldwin Ng’s current workplace is SiTime Inc., 5451 Patrick Henry Dr, Santa Clara, CA 95054, United States.

advantages: it's lead-free, allows for deposition at temperatures below 400°C, and is compatible with CMOS fabrication [10]. As reported in [21], [22], the SON process for pMUT microfabrication employs the migration of silicon to form a monocrystalline silicon (mono-Si) membrane over a buried cavity on 8-inch Silicon wafers. As a result, SON pMUTs can demonstrate low-cost, high-yield, and high fill-factor pMUT arrays [21], [22]. Furthermore, with the SON process, pMUT designs can be more flexible without lateral dimension limitations and the device fill-factor can be greatly increased compared to other common microfabrication methods [21], [22].

In our previous work, preliminary experimental imaging results with a 1D SON ScAlN pMUT linear array were presented considering the Common Source Method (CSM) for data acquisition and the Total Focusing Method (TFM) for image reconstruction [15]. In this paper, the work is further extended to demonstrate for the first time, the imaging capability over long ranges of a 2D SON ScAlN pMUT multi-channel array. There are two distinct differences in the work proposed in the present contribution as compared to [15]. Firstly, the utilization of a 2D pMUT array as opposed to a 1D array reported in [15] allows the ability for long-range imaging comfortably up to 4-5cm (with experimental results presented in this work covering 2-3cm in range). Secondly, the Common Source Method is replaced by a transmit (TX) beamforming scheme, which results in a much more focused acoustic beam-width. Hence, a better lateral resolution (5mm) has been demonstrated experimentally. The paper is organized as follows: Section II presents the SON pMUT design and some of its key characteristics quantified through hydrophone measurements. In addition, the 2D array configuration, experimental setup, actuation methodology, and data post-processing are discussed in detail. Section III covers three experimental scenarios to validate the 3D imaging capability of the proposed 2D array. Lastly, conclusions are drawn in Section IV.

II. PMUT Design Characteristics

A. Single pMUT chip design specifications & acoustic characterization

Figure 1a shows the optical image of a ScAlN pMUT array chip used in this work. Figure 1b depicts the SEM image of the pMUT array (upper figure) and the cross-section of the various layers that a SON pMUT element consists of along with the dimensions of each layer (lower figure). The pMUT array consists of 34×37 elements with a total aperture size of 7.03mm^2. The cavity width for each pMUT element (membrane) is 65µm, whereas the element pitch is 75µm (Fig. 1b). The 37×34 pMUT elements in the chip are split into two groups of 19×34 and 18×34 elements each (seen in Fig. 1a), with the rows and columns of each group electrically connected in parallel to form a single channel.

The pMUT array was split into two independent channels per die (in the above arrangement of 19×34 and 18×34) to

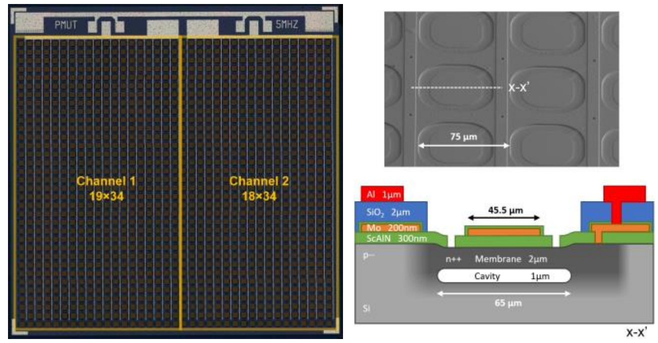

(a) (b)

Fig. 1. (a) Optical image of the 37×34 pMUT elements split into two channels in a chip; (b) Top image: SEM image of the pMUT array showing the pitch between adjacent pMUT element. Bottom image: illustration of the SON pMUT cross-section and dimensions.

ensure the impedance per channel is close to 50Ω at the device resonant frequency (5 MHz when operated in air) for maximum power delivery. The resonant frequency of the PMUT in air has been validated and reported in [21] (as R32.5 device in Fig. 4). The pMUT array fill factor corresponds to 66.3%. A cavity pitch equal to 10μm was chosen to ensure a 6μm wide electrical routing is sufficient to support the current needed to drive the pMUT array without the tracks burning during immersion test.

The immersion characterization of a single pMUT channel (aperture of 3.59mm^2) was carried out in a matching medium (FC-70) using a 40µm diameter hydrophone needle from Precision Acoustics Ltd. Figure 2 depicts the transmit sensitivity as a function of frequency from 0.1 to 10MHz at a distance of ~3.26cm above a single (half die) channel in log scale for the y-axis (rel. to 1 kPa/V). It can be seen from Fig. 2 that the maximum transmit sensitivity occurs approximately at 2.7MHz, which is the nominal frequency used to excite the 2D ScAlN array for the subsequent immersion imaging experiments discussed in Section III. The -3dB bandwidth for a pMUT channel, measured to be approximately 1.8MHz, will contribute towards better imaging resolution and imaging contrast enhancement, two significant requirements for obtaining high-quality images with pMUTs. Based on double beam laser interferometer measurements of the film with a thickness of 1μm, the e_{31f} coefficient is about 14-15 C/m^2). The coefficient is possibly slightly lower for the thinner film (0.3μm) reported in this work.

Furthermore, the field-of-view (FOV) for a single pMUT channel (i.e. half die) was measured using the aforementioned hydrophone setup. The hydrophone needle was moved after every measurement point to raster-scan the (x,z) space above the pMUT array and measure the received time-domain pressure. The pMUT channel was actuated with a 16Vpp 5-cycles sinusoidal wave at 2.7MHz. Figure 3 illustrates the pressure distribution above the pMUT array in the (x,z) plane. The pMUT array is located at the axis origin (0,0), whereas the FOV is defined as the angle between the element boresight axis and the axis to the point of half maximum power (corresponding to the full-width-half-maximum). Based on this

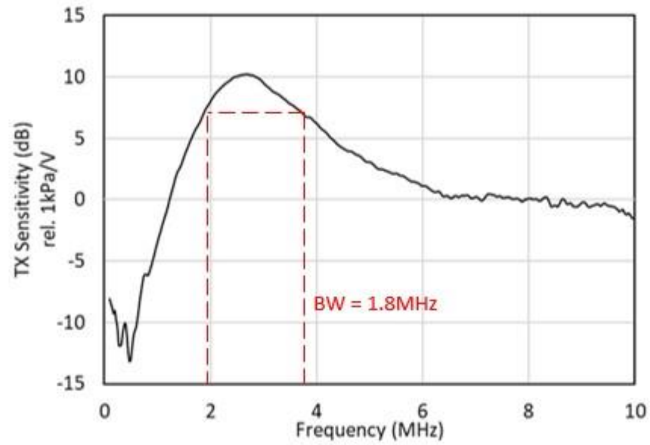

Fig. 2. Frequency sweep of pressure sensitivity of single channel pMUT array (aperture of 3.59mm²) in immersion with a hydrophone.

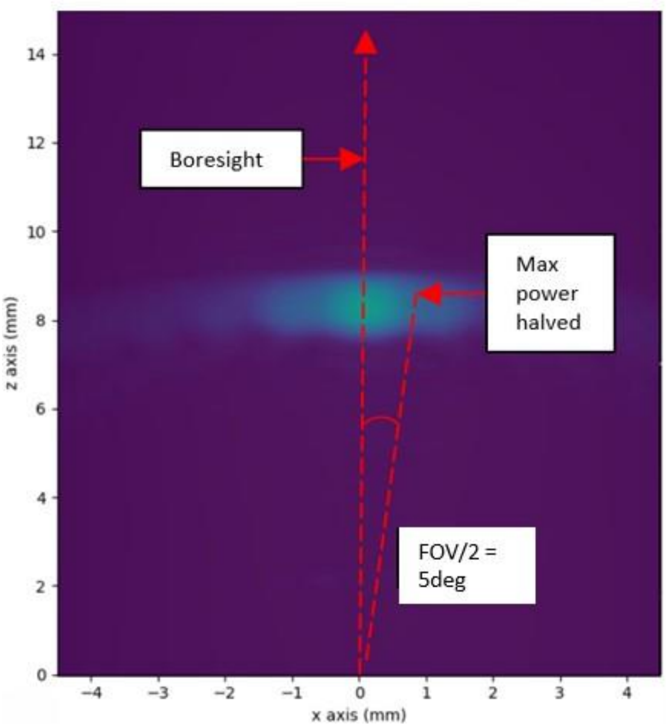

Fig. 3. Single channel pMUT array directivity pattern based on hydrophone measurement.

measurement, the FoV is conservatively determined to be 10°, indicating the directivity of a pMUT channel.

B. 2D Array Configuration and Experimental Setup

The 2D pMUT array configuration (depicted in Figure 4) consists of 16 dies arranged in two rows and eight columns on a custom-designed printed circuit board (PCB). Each die has 34×37 pMUT elements, which are split into two channels (seen in Fig. 1a), as discussed in Section II-A. Every chip was die-attached and wire bonded onto a PCB, as shown in Fig. 4. The bonding wires were encapsulated with epoxy to prevent damage during the experiment. Each pMUT channel was connected to a micro-coaxial port for interfacing with

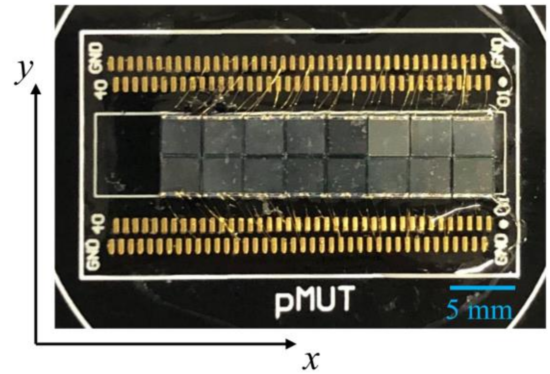

Fig. 4. Top view of the 32-channel ScAlN pMUT array composed of 16×2 pMUT chips wirebonded onto the PCB. The bonding wires were encapsulated to prevent damage during immersion.

the Verasonics system. It is worth noting that an evaluation of how various packaging methods may affect the imaging performance has not been conducted as part of this work. However, since the SON process does not use back-port etch to release the pMUT element membranes, the authors do not suspect any degradation/affect in the acoustic performance due to different die-attach/packaging methodologies.

Each chip has two channels with each channel mapped to an input/output (I/O) channel of a Verasonics Vantage™ 64 Research Ultrasound System. This results in a 2D 32-channel pMUT array configuration which can be individually (i.e., on a per channel basis) addressed and the received signal can be processed in real-time or offline. It is worth highlighting that the element structure in both the 1D SON ScAlN pMUT linear array reported by the authors in [15] and the 2D SON ScAlN pMUT array presented in this work are identical.

The device was submerged in 3M Fluorinert FC-70 fluid with an acoustic impedance equivalent to that of human tissue (~1.3MRayls). All the channels were excited simultaneously by pulsating with a 3-cycle 10Vpp sinusoidal signal at 2.7MHz using the Verasonics Vantage™ 64 Research Ultrasound System. A metal reflector with a diameter of 6mm was used in all the imaging experiments to validate the imaging capabilities of the multi-channel pMUT array in conjunction with the respective imaging algorithms.

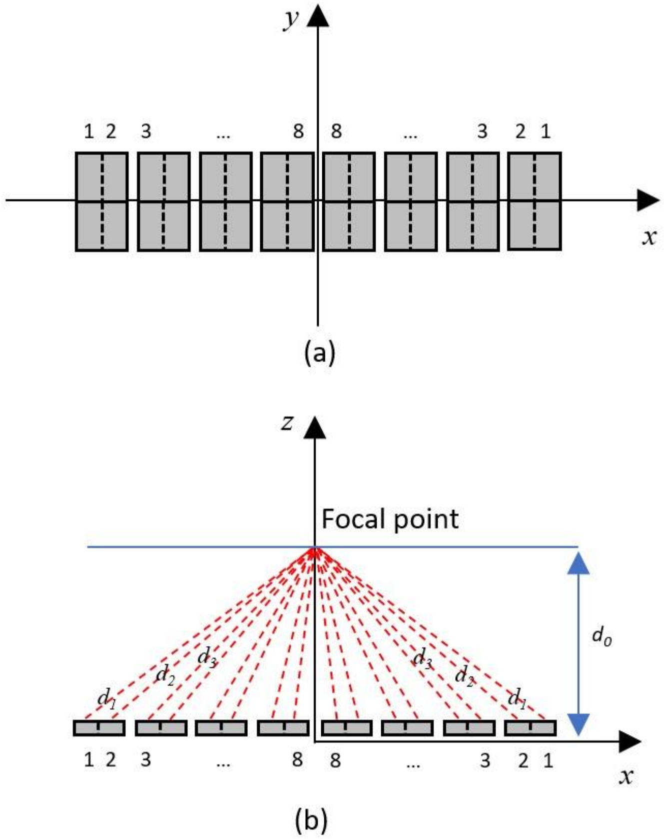

Fig. 5. (a) XY view plane of the 2D pMUT array die arrangement; (b) XZ view plane of the transmit beamforming. Note that for the experiments considered in this work, the focal distance, d_0, is tuned to a depth of 2.5cm.

C. Transmit (TX) Beamforming & Imaging Algorithm

Figure 5a illustrates the top view of the 2D pMUT array arrangement, whereas Figure 5b shows a diagram of the operation of the transmit (TX) beamforming for this array. When considering TX beamforming, a time delay is applied to the transmit waveform for every channel to create a time-delay beamforming effect. This allows the transmitted beam to focus at a specific point in the propagation medium (known as the focal point). As seen in Fig. 5b, the center of a channel is taken as the origin for each of the 2×16 channels. With this as the reference point, a time delay, τ, is applied to the excitation signal of channels 1–8 (considering the array symmetry along the x-axis) with the following relationship:

$$\tau_i = \frac{d_i - d_0}{c} \quad (1)$$

where i corresponds to the i-th channel of the 2D array; d_0 corresponds to the Euclidean distance between the origin of the multi-channel array and the focal point; d_i refers to the Euclidean distance between the origin of the i-th channel and the focal point; and c is the speed of sound in the propagation medium. The focused beam diameter is dependent on the array aperture, which corresponds to the number of dies (i.e. 8 along the lateral dimension) multiplied by their pitch (i.e., die pitch of ~3.2mm).

Hypothetically, when the focused acoustic beam impinges on the surface of a reflector, the out-of-phase (delayed) echo signals are reflected to the array. The acoustic pressure received by the array channels will be converted to electrical signals, which will be captured and analyzed by the Verasonics System. Figure 6 depicts the post-signal processing of the received raw signals, $y_n(t)$, to obtain the final reconstructed 3D image.

The time delay of each channel calculated by (1) is applied to the out-of-phase (delayed) received signals to obtain the in-phase (time-aligned) echo signals. After the time alignment, the signals are passed to the received beamforming algorithm in order to reconstruct a 3D image. This image would correspond to the distribution of energy intensity on a 3D Cartesian grid of finite-spaced points (referred to as pixels) which maps all the possible reflector locations in the imaging domain. For every pixel, all the in-phase received signals are time-shifted by $2d_{\text{pixel(rx)}}/c$ and then summed with the overall operation of the imaging algorithm expressed by the following equation:

$$I(x_{\text{pixel}}, y_{\text{pixel}}) = \left| \sum y_{\text{rx}} \left(\tau_i + \frac{2d_{\text{pixel(rx)}}}{c} \right) \right| \quad (2)$$

where $d_{\text{pixel(rx)}}$ corresponds to the Euclidean distance from the pixel to the receiving (RX) channel - with multiplication by 2 referring to the round-trip distance; $y_{\text{rx}}(t)$ is the received out-of-phase signal recorded at every rx channel; c corresponds to the known speed of sound in the propagation medium; and τ_i refers to the time-delay applied to every i-th channel of the array during actuation computed from eq. (1). The location of each focal point is known in advance since it is needed for the beam to focus from the transmit side. The pMUT directivity is also incorporated in the post-processing to ensure that the narrow pMUT FoV is taken into account in the final imaging result.

Once time-shifted, all the received signals are summed. This way, the signal contributions corresponding to the reflector constructively add resulting in an increased energy intensity value for a specific pixel(s), whereas the ones corresponding to noise or other undesired (non-static) signal contributions are canceled out or result in a minimal energy intensity value for some of the pixels. The final absolute value of energy intensity is assigned to the pixel and the process is repeated for the next pixel in the 3D grid until all pixels are assigned a value of absolute energy intensity. The final 3D image is normalized by the maximum intensity within the 3D grid.

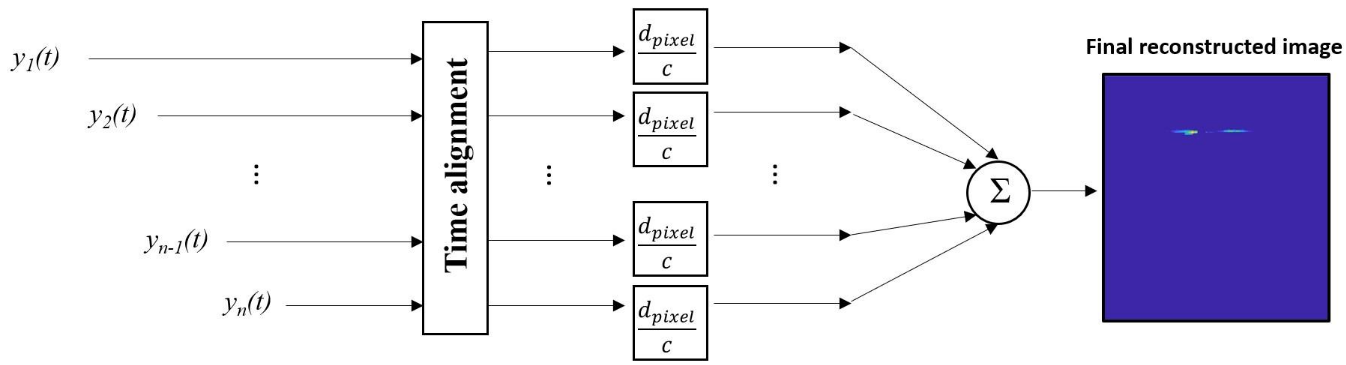

Fig. 6. Received (RX) beamforming signal processing.

III. Experimental Validation

As previously mentioned, metal reflectors with a diameter of 6mm were used to validate the imaging capabilities of the 2D ScAlN pMUT array in immersion. Three experiments with different reflector arrangements were carried out. Figure 7 depicts the overall experimental setup used for testing and the three test scenarios (denoted as A, B, and C).

The TX beamforming scheme (discussed in Section II-D and denoted as ”focused imaging” for the remaining of this document) was compared against the Common Source Method (CSM), whereby all array channels are excited simultaneously followed by RX beamforming (i.e. classical TFM) processing (denoted as ”unfocused imaging” hereinafter). A detailed description of the CSM excitation scheme is reported in [26]. In terms of visualizing the 3D imaging results, once the normalized 3D image of energy intensity is obtained, the (x,y,z) co-ordinates of the pixel with maximum intensity in the 3D image are determined and used to slice through the (x,z) and (x,y) planes to generate two 2D images.

The sequence of the experiments is as follows: First, a single 6mm diameter reflector is considered (Experiment A) to validate the proposed focused imaging scheme contrasted against the unfocused imaging scheme. Experiment A is used to determine the energy intensity threshold that would result in optimal 2D images and is, thus, treated as an experiment for the calibration of the energy intensity threshold. In Experiment B, a second identical reflector is added with the spacing between the two reflectors being set to 1.5cm providing a basis for the lateral resolution given the selected intensity threshold(s) in the 2D images. Finally, Experiment C challenges the imaging capability of the system by bringing the two reflectors closer to each other (at a distance of 0.5cm) and investigating whether the two reflectors can be resolved by the system with either focused or unfocused imaging. Note that for all the experiments, the reflector(s) were placed at a fixed distance from the 2D array of 2.5cm.

For all the results presented, the FoV in the imaging algorithm was set to 10° to closely match the measured pMUT FoV (shown in Fig. 3). Given that only a certain number of pixels will fall within the narrow directivity (FoV) of every array channel, the resulting 2D images will be discretized. This discretization effect will result in coarse energy intensities at the location of the reflector, as opposed to the case whereby omnidirectionality (360° FoV) was assumed and all the pixels were considered by every array channel, which would result in images of smooth energy intensity at the location of the reflector.

A. Experiment A: Calibration of energy intensity

In this scenario, a single 6mm diameter reflector was placed above the center of the 2D array. Figure 7 shows the experimental setup along with the fluid-filled tank and submerged pMUT array. Initially, all the pixels are depicted considering a normalized intensity range of 0-1. However, in clinical modalities, the intensity tends to be modified by clinicians through the use of an intensity threshold slider. In order to replicate this to an extent, a threshold value is applied to the results, which defines the lower limit of intensity to be included in the 2D reconstructed images. The lower limit threshold values of 0, 0.5, 0.6, and 0.7 were investigated to compare the final reconstructed images.

Figure 8 depicts the 2D imaging results obtained using the unfocused imaging scheme (row 1 for (x,z) plane images, row 2 for (x,y) plane images - highlighted in blue) and the focused imaging scheme (row 3 for (x,z) plane images and row 4 for (x,y) plane images - highlighted in maroon) for the considered energy intensity threshold values (labeled for each column). It can be observed that a fairly equivalent reconstruction of the reflector is obtained with both focused and unfocused imaging schemes when no energy intensity threshold is being applied (first column in Fig. 8).

By observing the results for the intensity threshold values of 0.5, 0.6 and 0.7 (seen in second, third and fourth columns respectively in Fig. 8), it can be said that the reconstruction of the reflector in the (x,z) plane is optimized, with the resulting energy concentration closely mapping the actual dimension of the reflector for the 0.5 and 0.6 threshold values. The 0.7 threshold leads to a significant reduction in the energy content within the 2D images for both imaging schemes. Hence, the imaging results considering the intensity threshold values of 0.5 and 0.6 alone will be considered in the next experiment as they provide a better reconstruction of the reflector.

B. Experiment B: Two reflectors 1.5cm apart

In this scenario, two 6mm diameter reflectors were attached to the 3D printed holder at a distance of approximately 1.5cm from each other to investigate the lateral resolution that can be achieved by the proposed pMUT array with focused imaging. Fig. 7 shows a close-up image of this experimental setup. The distance of 1.5cm between the two reflectors was selected on the basis that it enables both reflectors to be in the coverage area of the 2D array and, therefore, comfortably imaged by it.

Figure 9 depicts the 2D imaging results in the (x,z) and (x,y) planes for the unfocused and focused imaging, considering the energy intensity threshold values of 0.5 and 0.6. It can be argued that the two reflectors can be clearly separated in the imaging result when focused imaging is considered and

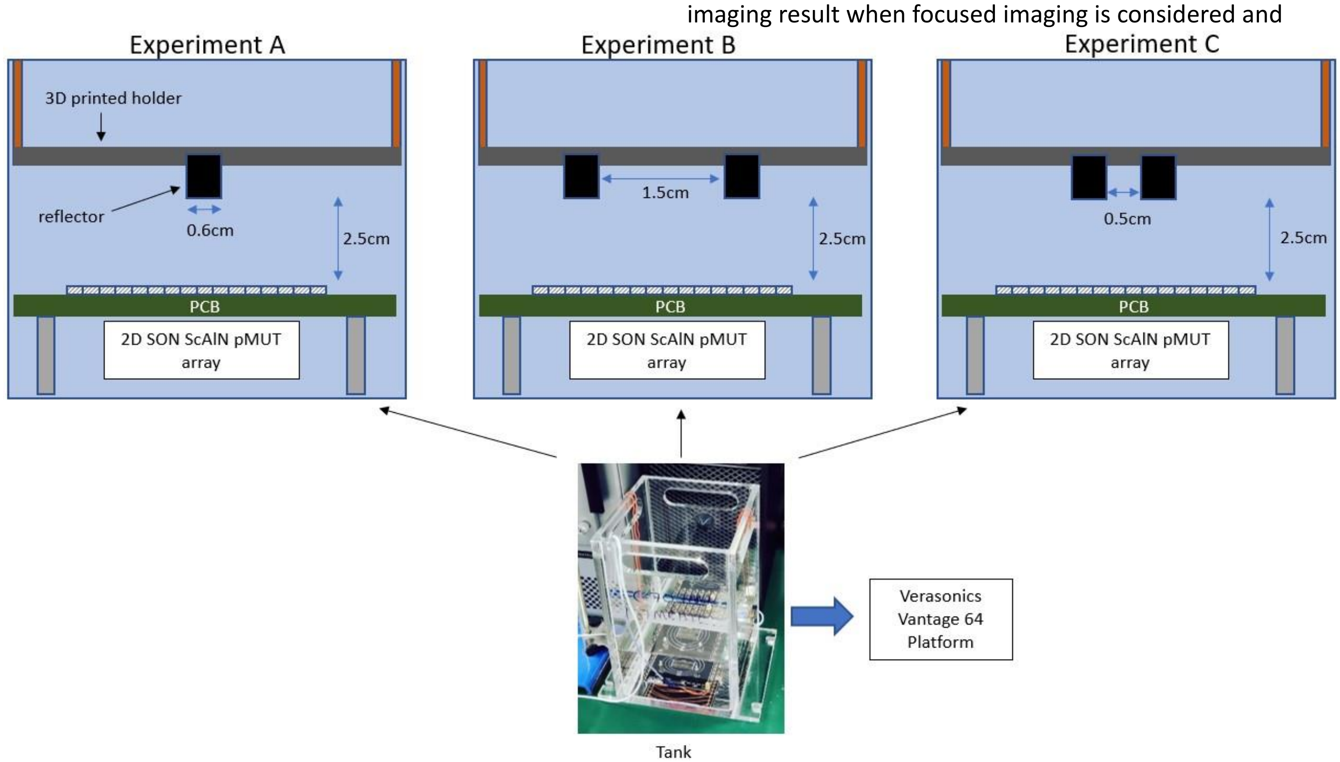

Fig. 7. Experimental setup for the three imaging scenarios. Experiment A consists of single 6mm diameter reflector placed 2.5cm above the array. Experiment B consists of two 6mm diameter reflectors placed 1.5cm apart and 2.5cm above the array. Experiment C consists of two 6mm diameter reflectors placed 0.5cm apart and 2.5cm above the array.

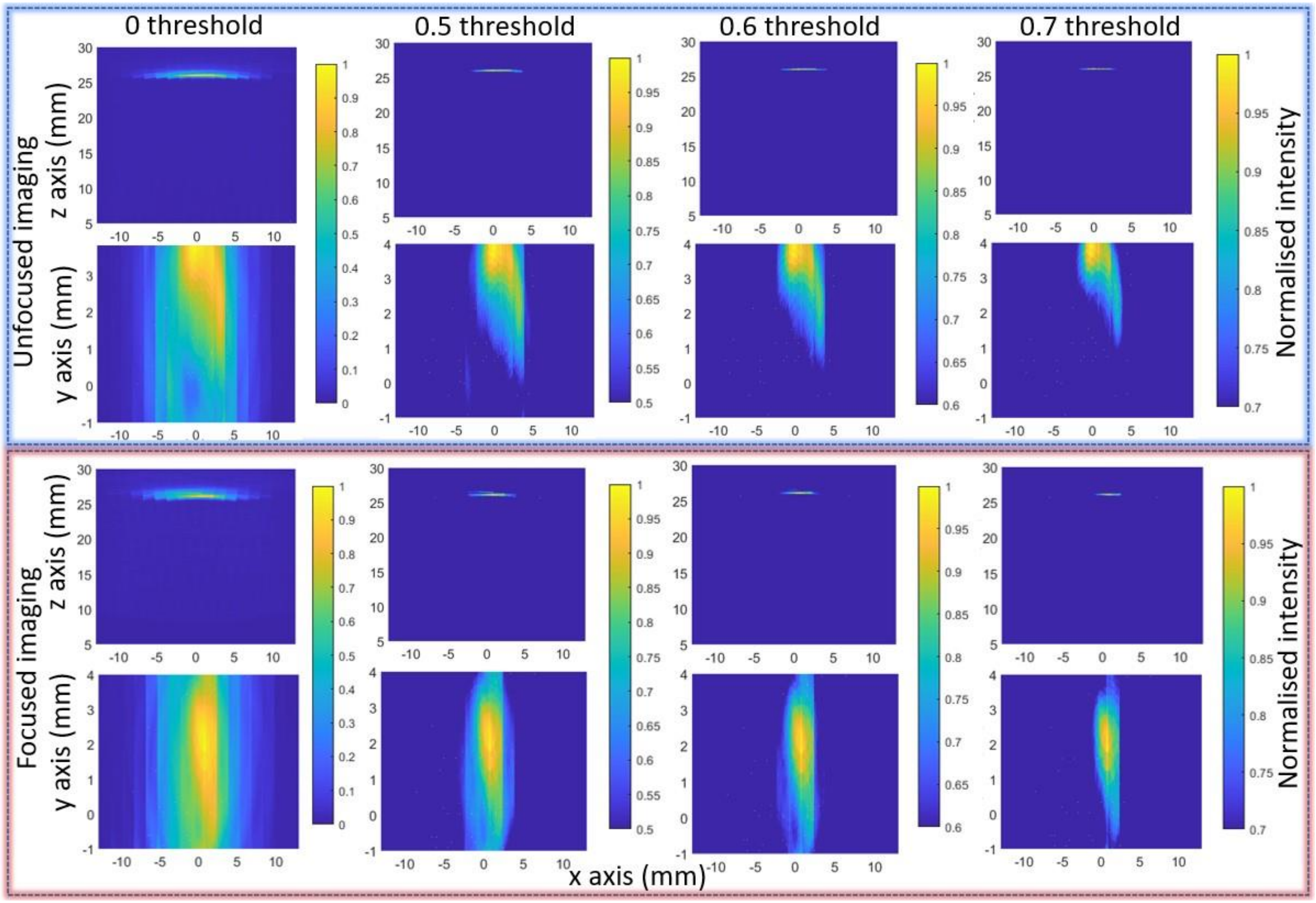

Fig. 8. Reconstructed image of experiment A sliced along the (x,z) and (x,y) planes with normalized pixel intensity using unfocused imaging and focused imaging. Each column corresponds to energy intensity thresholds of 0, 0.5, 0.6 and 0.7.

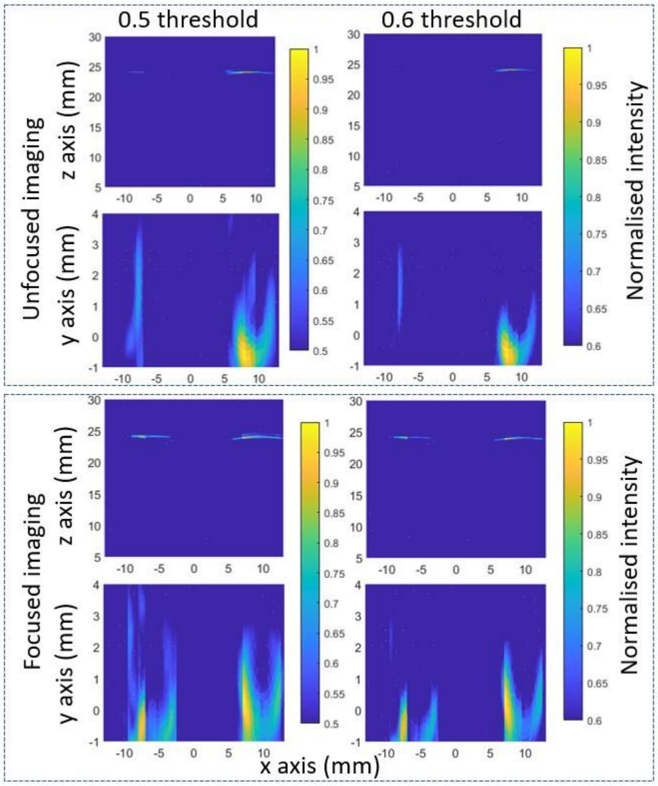

Fig. 9. Reconstructed image of experiment B sliced along the (x,z) and (x,y) planes with normalized pixel intensity using unfocused imaging and focused imaging. Each column corresponds to energy intensity thresholds of 0.5 and 0.6.

the energy intensity threshold is equal to either 0.5 or 0.6. Unfocused imaging is unable to resolve the two objects in proximity when using either 0.5 or 0.6 threshold for the energy intensity.

Based on the results presented so far in Sections III-A and III-B, it can be argued that the focused imaging scheme outperforms the unfocused imaging scheme as both reflectors can be resolved irrespective of the energy intensity threshold being 0.5 or 0.6. The superiority of focusing imaging in the lateral resolution is primarily attributed to the narrow TX beam-width. Given that the threshold value of 0.5 provides a better representation of the location of the two reflectors, this threshold value will be considered in the next experiment.

C. Experiment C: Two reflectors 0.5cm apart

In this scenario, the two 6mm diameter reflectors were placed closer, at approximately 5mm to further challenge the lateral resolution that is achievable with the proposed array and focused imaging scheme. Fig. 7 shows the experimental setup for experiment C. Figure 10 depicts the 2D imaging results in the (x,z) and (x,y) planes considering unfocused and focused imaging respectively with the obtained imaging results having an energy intensity threshold of 0.5. It can be argued that the two reflectors cannot be resolved when considering the unfocused imaging scheme. On the contrary, with focused imaging, the two reflectors can be clearly identified as two distinct objects. It can be concluded that the proposed pMUT

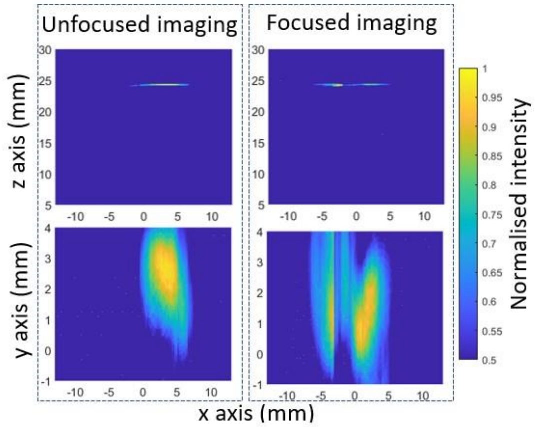

Fig. 10. Reconstructed image of experiment B sliced along the (x,z) and (x,y) planes with normalized pixel intensity using unfocused imaging and focused imaging. Each column corresponds to energy intensity threshold of 0.5.

array arrangement can achieve comfortably a lateral resolution of 5mm when using TX beamforming.

The theoretical maximum lateral resolution given an array aperture size of 40.84mm (corresponding to 8 pMUT dies in the configuration specified in Section II-A) and an actuation frequency of 2.7MHz is computed to be circa 0.2mm when considering focusing at 2.5cm above the array. In order for this optimum resolution to be achieved, the following considerations on the pMUT array design should be taken into account: (i) the intra-die spacing should be uniform, and (ii) every pMUT die should have a maximum fill-factor to ensure that the membrane pitch among dies (of such a multi-die pMUT array) remains uniform for the length of the pMUT array along its lateral dimension.

Figure 11 depicts the received time-domain waveform obtained at array element 20 for the unfocused methodology, whereas Figure 12 depicts the equivalent time-domain response for the same array element considering the focused imaging method. By comparing Fig. 11 and 12, it can be argued that the time-domain waveform for the focused method better represents the two reflectors as opposed to the time-domain response for the unfocused method. This is attributed to the narrow TX beamwidth achieved with the TX beamforming.

D. Discussion

Although the current pMUT array and actuation scheme can easily achieve high-quality imaging at a distance of 2.5cm, this range could be further improved empirically; which we have indeed verified. This includes doubling the range to 5cm, through the use of higher AC actuation (i.e. 20Vpp) and/or the introduction of amplification at the receiving end prior to post-processing for image reconstruction. However, to extend the imaging range further, to say 10cm, the increase of the actuation voltage would be higher and/or a lower frequency of operation would be considered given that as the wavelength is increased (or frequency decreased) the ultrasound will penetrate deeper. Obviously, the change in

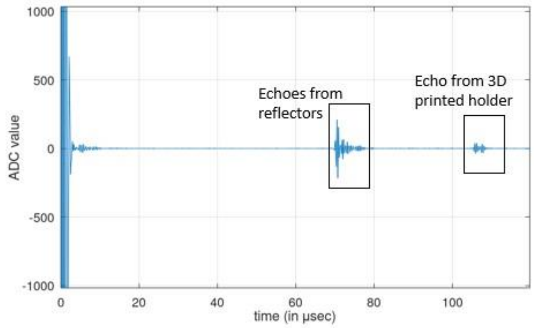

Fig. 11. Received time-domain response for the unfocused imaging approach

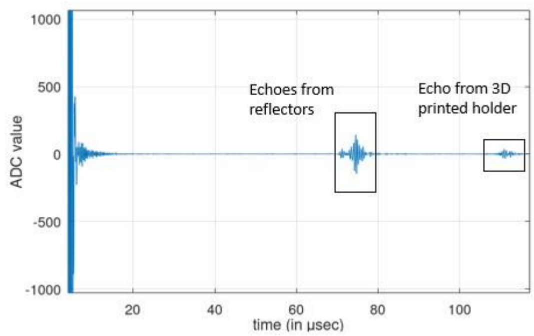

Fig. 12. Received time-domain response for the focused imaging approach

frequency of operation would have implications on the design characteristics of the array itself. Equally, increasing the actuation voltage, through the use of amplification, would pose challenges in terms of pMUT elements being burned/damaged (as it was again identified empirically).

Future considerations of this work would also include enhancing the lateral resolution towards the theoretical limit of 0.2mm. This could be reached through re-design of the 32-channel pMUT array such that the element pitch of 75µm remains constant from channel to channel among the different dies used to construct the multi-channel pMUT array. Finally, the signal-to-noise ratio (SNR) could also be improved through the introduction of more channels in the array; for the 2-row 8-die arrangement considered here, the definition of 37 channels per die with 34 membranes each would result in 592 (37 channels/die × 8 dies/row × 2 rows) received signals compared to the 32 received signals in the existing multi-channel pMUT array arrangement.

IV. Conclusion

The work presented here aims at filling the gap in the literature in immersion imaging at long ranges (>2cm) with pMUTs and showcasing the imaging capabilities of a 2D SON pMUT array with a 15% Scandium doped Aluminum Nitride (ScAlN) thin film. In practice, this work demonstrates the use of a 2×16-channel 2.7MHz ScAlN pMUT array for immersion pulse-echo imaging using transmit (TX) beamforming (i.e. TX focusing) with the proposed 32-channel 2D pMUT array and imaging scheme having the ability to resolve adjacent 6mm diameter reflectors as close as 5mm defining a milestone in lateral resolution at long-range imaging in immersion with ScAlN pMUT arrays. This actuation mechanism (TX beamforming) provides a significant advantage in lateral resolution compared to the case of actuating the array with an unfocused excitation waveform. This would be attributed to the narrow focus beam-width enabled by TX beamforming. A further contributor to the high-quality images claimed in this work is the wide -6dB bandwidth (equal to 2.9MHz) that can be attained with the aforementioned pMUT array.

The results presented in this work indicate that the pMUT array has great potential for applications towards imaging in fluids such as the navigation of autonomous underwater vehicles (AUVs) and as a priori information for subsequent targeted imaging (i.e., via beam focusing or steering) for medical imaging towards detection or targeted therapeutic imaging.

Acknowledgment

This research was supported by A*STAR under the “Piezo Specialty Lab-in-a-Fab” (Grant No. I1901E0050) and “Nanosystems at the Edge” programme (Grant No. A18A4b0055)

References

[1] W. Lee and Y. Roh, “Ultrasonic transducers for medical diagnostic imaging,” *Biomedical engineering letters*, vol. 7, no. 2, pp. 91–97, 2017.

[2] C. Holmes, B. W. Drinkwater, and P. D. Wilcox, “Post-processing of the full matrix of ultrasonic transmit–receive array data for non-destructive evaluation,” *NDT & e International*, vol. 38, no. 8, pp. 701–711, 2005.

[3] Z. Qiu, Y. Lu, and Z. Qiu, “Review of ultrasonic ranging methods and their current challenges,” *Micromachines*, vol. 13, no. 4, p. 520, 2022.

[4] Y. Koh, D. S. W. Choong, D. S.-H. Chen, D. J. Goh, S. Ghosh, J. Sharma, S. Merugu, F. Quaglia, M. Ferrera, A. S. Savoia *et al.*, “High resolution, high frequency ultrasonic ranging in air with pmuts,” in *2021 IEEE International Ultrasonics Symposium (IUS)*. IEEE, 2021, pp. 1–4.

[5] I. Rakkolainen, E. Freeman, A. Sand, R. Raisamo, and S. Brewster, “A survey of mid-air ultrasound haptics and its applications,” *IEEE Transactions on Haptics*, vol. 14, no. 1, pp. 2–19, 2020.

[6] J. Jung, W. Lee, W. Kang, E. Shin, J. Ryu, and H. Choi, “Review of piezoelectric micromachined ultrasonic transducers and their applications,” *Journal of Micromechanics and Microengineering*, vol. 27, no. 11, p. 113001, 2017.

[7] W. Ji, L. Liu, Z. Xing, D. Zhang, Y. Wang, L. Chen, Y. Chen, X. Sun, and Y. Du, “Total-focus ultrasonic imaging of defects in solids using a pzt piezoelectric micromachined ultrasonic transducer array,” *IEEE Transactions on Ultrasonics, Ferroelectrics, and Frequency Control*, vol. 68, no. 4, pp. 1380–1386, 2020.

[8] Y. Qiu, J. V. Gigliotti, M. Wallace, F. Griggio, C. E. Demore, S. Cochran, and S. Trolier-McKinstry, “Piezoelectric micromachined ultrasound transducer (pmut) arrays for integrated sensing, actuation and imaging,” *Sensors*, vol. 15, no. 4, pp. 8020–8041, 2015.

[9] O. Rozen, S. T. Block, X. Mo, W. Bland, P. Hurst, J. M. Tsai, M. Daneman, R. Amirtharajah, and D. A. Horsley, “Monolithic mems-cmos ultrasonic rangefinder based on dual-electrode pmuts,” in *2016 IEEE 29th International Conference on Micro Electro Mechanical Systems (MEMS)*. IEEE, 2016, pp. 115–118.

[10] Y. Lu, A. Heidari, and D. A. Horsley, "A high fill-factor annular array of high frequency piezoelectric micromachined ultrasonic transducers," *Journal of Microelectromechanical Systems*, vol. 24, no. 4, pp. 904–913, 2014.

[11] Y. Lu, O. Rozen, H.-Y. Tang, G. L. Smith, S. Fung, B. E. Boser, R. G. Polcawich, and D. A. Horsley, "Broadband piezoelectric micromachined ultrasonic transducers based on dual resonance modes," in *2015 28th IEEE International Conference on Micro Electro Mechanical Systems (MEMS)*. IEEE, 2015, pp. 146–149.

[12] J. Jung, S. Kim, W. Lee, and H. Choi, "Fabrication of a two-dimensional piezoelectric micromachined ultrasonic transducer array using a top-crossover-to-bottom structure and metal bridge connections," *Journal of Micromechanics and Microengineering*, vol. 23, no. 12, p. 125037, 2013.

[13] Y. Lu, H.-Y. Tang, S. Fung, B. E. Boser, and D. A. Horsley, "Pulse-echo ultrasound imaging using an aln piezoelectric micromachined ultrasonic transducer array with transmit beam-forming," *Journal of Microelectromechanical Systems*, vol. 25, no. 1, pp. 179–187, 2015.

[14] Y. Lu, H. Tang, Q. Wang, S. Fung, J. M. Tsai, M. Daneman, B. E. Boser, and D. A. Horsley, "Waveguide piezoelectric micromachined ultrasonic transducer array for short-range pulse-echo imaging," *Applied Physics Letters*, vol. 106, no. 19, p. 193506, 2015.

[15] M. Sarafianou, D. S. W. Choong, D. J. Goh, D. S.-H. Chen, and Y. Zhang, "A csm/tfm imaging scheme for silicon-on-nothing scaln pmut array," in *2022 IEEE International Ultrasonics Symposium (IUS)*. IEEE, 2022, pp. x–x.

[16] K. Smyth, C. Sodini, and S.-G. Kim, "High electromechanical coupling piezoelectric micro-machined ultrasonic transducer (pmut) elements for medical imaging," in *2017 19th International Conference on Solid-State Sensors, Actuators and Microsystems (TRANSDUCERS)*. IEEE, 2017, pp. 966–969.

[17] Y.-F. Wang, T.-L. Ren, Y. Yang, H. Chen, C.-J. Zhou, L.-G. Wang, and L.-T. Liu, "High-density pmut array for 3-d ultrasonic imaging based on reverse-bonding structure," *2011 IEEE 24th International Conference on Micro Electro Mechanical Systems*, pp. 1035–1038, 2011.

[18] B. Chen, F. Chu, X. Liu, Y. Li, J. Rong, and H. Jiang, "Aln-based piezoelectric micromachined ultrasonic transducer for photoacoustic imaging," *Applied Physics Letters*, vol. 103, no. 3, p. 031118, 2013.

[19] Y. Lu, S. Shelton, and D. A. Horsley, "High frequency and high fill factor piezoelectric micromachined ultrasonic transducers based on cavity soi wafers," in *Proc. Solid-State Sensors, Actuators and Microsystems Workshop*, 2014, pp. 131–134.

[20] H.-Y. Tang, Y. Lu, S. Fung, D. A. Horsley, and B. E. Boser, "11.8 integrated ultrasonic system for measuring body-fat composition," in *2015 IEEE International Solid-State Circuits Conference-(ISSCC) Digest of Technical Papers*. IEEE, 2015, pp. 1–3.

[21] D. S. W. Choong, D. S.-H. Chen, D. J. Goh, J. Liu, S. Ghosh, Y. Koh, J. Sharma, S. Merugu, F. Quaglia, M. Ferrera *et al.*, "Silicon-on-nothing scaln pmuts," in *2021 IEEE International Ultrasonics Symposium (IUS)*. IEEE, 2021, pp. 1–4.

[22] J. Sharma, D. J. Goh, S. Merugu, Y. Koh, S. Ghosh, M. H. Khairy, and E. J. Ng, "Piezoelectric over silicon-on-nothing (pson) process," in *2021 IEEE International Ultrasonics Symposium (IUS)*. IEEE, 2021, pp. 1–4.

[23] A. Hajati, D. Latev, D. Gardner, A. Hajati, D. Imai, M. Torrey, and M. Schoeppler, "Three-dimensional micro electromechanical system piezoelectric ultrasound transducer," *Applied Physics Letters*, vol. 101, no. 25, p. 253101, 2012.

[24] M. Sarafianou, D. J. Goh, and D. S. W. Choong, "A tof estimation algorithm for ranging using silicon-on-nothing pmuts," in *2022 IEEE International Ultrasonics Symposium (IUS)*. IEEE, 2022, pp. x–x.

[25] P. Muralt, "Pzt thin films for microsensors and actuators: Where do we stand?" *IEEE transactions on ultrasonics, ferroelectrics, and frequency control*, vol. 47, no. 4, pp. 903–915, 2000.

[26] L. Moreau, B. W. Drinkwater, and P. D. Wilcox, "Ultrasonic imaging algorithms with limited transmission cycles for rapid nondestructive evaluation," *IEEE Transactions on Ultrasonics, Ferroelectrics, and Frequency Control*, vol. 56, no. 9, pp. 1932–1944, 2009.

Mantalena Sarafianou is a Scientist at the Institute of Microelectronics (IME), a research institute of the Agency for Science, Technology and Research (A*STAR) in Singapore. Her current research interests are in signal processing applications for ultrasonic miniaturized sensors. Dr Sarafianou has experience of working as an R&D engineer, specialising in the development of signal processing solutions for a wide range of industries such as medical devices, consumer electronics, and automotive.

Dr Sarafianou is an alumna of the University of Bristol, where she obtained a postgraduate degree in Communication Systems and Signal Processing (MSc: 2008), and a doctorate in in Electrical and Electronic Engineering (PhD: 2012), and the Aristotle University of Thessaloniki, Greece, where she completed her undergraduate degree in Electrical and Computer Engineering (2007).

David Sze Wai Choong graduated from the National University of Singapore with a Honours degree, Bachelor of Engineering (Mechanical) in 2015 and proceeded to work in the semiconductor manufacturing industry for 2 years before joining A*STAR, Institute of Microelectronics (IME) in 2017. He has spent 3 years in the MedTech department working on miniaturized medical devices on silicon for catheter integration and on flexible electronics and sensor integration for biomedical, applications. Currently, he is working under the sensors, actuators and microsystems (SAM) department and acoustics group to further research MEMs PMUT devices in terms of performance testing, data analysis and prototyping applications.

Daniel Ssu-Han Chen (Member, IEEE) received the B.E. degree in electrical and electronics engineering from the University of Auckland, Auckland, New Zealand, in 2010, and the M.Eng.Sc. and Ph.D. degrees in electrical engineering from the University of New South Wales, Sydney, Australia, in 2013 and 2018, respectively. He was a Research Associate with University of New South Wales, Sydney, Australia in 2018. He is currently a Scientist with the Institute of Microelectronics, Agency for Science, Technology and Research (A*STAR), Singapore. His research interests include piezoelectric microelectromechanical systems (MEMS) actuators, acoustic MEMS, CMOS-MEMS integration, heterogeneous integration, micro/nano sensors, and flexible sensors.

Duan Juan Goh is a research engineer at Institute of Microelectronics, Agency for Science, Technology and Research (A*STAR).

He graduated from Nanyang Technological University with degree in Mechanical Engineering in 2020. Despite being fairly new to the field, his research work has involved testing related studies in MEMS technology, including pMUTs, resonators, wake-up sensor switches.

Zhang Yao received the B.Eng. (Hons) in Electrical and Electronic Engineering from Nanyang Technological University, Singapore (NTU) in 2005 and M.S. in Electrical Engineering from National University of Singapore, Singapore (NUS) in 2009.

From 2005 to 2010, she worked on automobile audio and video entertainment product development at JVC Electronics Singapore. From 2010 to 2011, she worked on business inject printer product development at Hewlett-Packard Singapore. From 2011 to 2016, she was with Data Storage Institute (A*STAR), Singapore and worked on drive technology and research development. Since 2016, she has been working at Institute of Microelectronics (A*STAR), Singapore. Her current work focus on sensors and actuators system-level prototyping.

Jaibir Sharma received his M.Sc. degree in physics from Chaudhary Charan Singh University, Meerut, India, in 1995, and the M.Tech. degree in solid state technology and the Ph.D. degree in electrical engineering from the Indian Institute of Technology (IIT) Madras, Chennai, India, in 2000 and 2010, respectively. He was involved in both industry and teaching before pursuing the Ph.D. degree at IIT Madras in 2004. From March 2010 to December 2010, he was a Post-Doctoral Fellow with Koc¸ University, Istanbul, Turkey.

He own more than 15 years' experience in MEMS integration area. He is working with the Institute of Microelectronics, Singapore as a MEMS integration Scientist from last 10 years. In IME, he integrated AlN and ScAlN based MEMS devices such as pressure sensor, FBAR filters and actuators, monolithic integration of pMUT on CMOS for finger print application, integration of AlN and ScALN on dual side of wafer for wavefront application. He established Polysilicon TSI process and encapsulation for MEMS devices. He also worked as a module owner for STS PECVD and developed many recipes for low temperature a-Si, oxide and nitride, especially tunable low stress SiN recipe. He published more than 15 technical papers in international journal and presented many papers in international conferences and symposiums. He has 10+ patents and know-hows.

His current research interests include MEMS reliability, cost-effective MEMS techniques, eutectic and fusion bonding, MEMS modeling, optical MEMS, thin-film encapsulation for MEMS devices, and integration of MEMS with CMOS devices.

Srinivas Merugu is a Senior researcher in MEMS Integration Group, Institute of Microelectronics, Agency for Science, Technology and Research (A*STAR), Singapore. His current research interests include piezoelectric-based microelectromechanical systems (MEMS) devices, such as resonators, hydrophones, piezoelectric micromachined ultrasonic transducers, and Bio-MEMS, in particular, neuroprosthetics and micrototal analysis systems.

Eldwin Jiaqiang Ng received the B.S. degree in mechanical engineering from the University of California, Berkeley in 2009, and the M.S. and Ph.D degrees in mechanical engineering from Stanford University in 2012 and 2015, respectively, with a focus on MEMS resonators. From 2015 to 2017, he worked on ultrasonic sensors at InvenSense, Inc., San Jose, CA, USA. From 2017 to 2021 he was with the Institute of Microelectronics (A*STAR), Singapore. He is currently at SiTime Corp, Santa Clara, CA, USA. His research interests include microfabrication technologies, resonators, and MEMS sensors.

Joshua En-Yuan Lee (Member, IEEE) Joshua En-Yuan Lee received both the B.A. and M.Eng. degrees in 2005, and the Ph.D. degree in 2009 from the University of Cambridge, U.K. He was previously an Associate Professor with the Department of Electrical Engineering, City University of Hong Kong. He was also a Visiting Professor with University Grenoble Alpes, France, in 2017. He is currently a Principal Scientist with the Institute of Microelectronics, A*STAR, Singapore. His research interests include piezoelectric microelectromechanical systems (MEMS) for imaging, sensing, wireless sensor nodes, and actuators. He has served on the technical program committees for various conferences, including ISQED, IFCS/EFTF, and Transducers.